# Accurate Micro-Doppler Analysis by Doppler and $k$-Space Decomposition for Millimeter Wave Short-Range Radar

Takeru Ando and Shouhei Kidera, *Senior Member, IEEE*

***Abstract*—This study presents a highly accurate range and Doppler-velocity extraction scheme for millimeter-wave (MMW) short-range sensing using the Doppler-velocity and $k$-space decomposition in a weighted kernel density (WKD) scheme. The WKD method has been developed as one of the most promising micro-Doppler analysis methods for human motion; however, an original WKD method requires a highly decomposed range profile to achieve its maximum performance. As the main contribution of this article, the proposed method introduces the Doppler velocity and k-space decomposition via the 4-D fast Fourier-transform process, which significantly improves the range resolution and reduces computational complexity. The numerical and experimental results show that the proposed method achieves significantly higher range and velocity accuracy and resolution, as well as higher noise-robustness at a lower computational cost.**

***Index Terms*—Human recognition radar, micro-Doppler analysis, millimeter wave (MMW) radar, pulse-Doppler radar, radar signal processing.**

## I. Introduction

MILLIMETER wave (MMW) radars are considered as suitable sensors for challenging conditions such as bad weather, nonline-of-sight situation [1], dense smog, or wall-through imaging [2]–[5]. In particular, human walking motion recognition is significantly important in the fields of advanced driver-assistant systems and security and rescue scenarios, where the gait level of the human body can be recognized from the reflection response features [6]. The micro-Doppler signature is one of the most promising features for recognizing the gait level of human motion. A large number of studies focusing on these systems [7]–[11] have been reported in the literature in recent years. Most of the micro-Doppler analyses are based on a coherent integration scheme such as the short-time Fourier-transform (STFT) [12]–[15], the Fourier-Bessel transform [16], the Wigner–Ville distribution [17], or the pseudoWigner distribution (SPWD) [18]. However, the above methods suffer from a limitation in the temporal and Doppler-velocity resolutions and also the unambiguous velocity range, which is strictly determined by the pulse repetition interval (PRI) and the carrier frequency wavelength. Furthermore, in assuming pulse-Doppler or frequency modulated continuous wave (FMCW) radar to obtain range and velocity profiles, the range walk (RW) effect may reduce the effective resolution because the reflection pulses move beyond the range resolution during the coherent processing interval (CPI) [19]. Many solutions have been developed for the RW issue such as the Radon Fourier transform (RFT) [20], the Radon fractional Fourier transform (RFRFT), the Hough transform (HT) [21]–[23], the keystone transform [24]–[26], or the discrete polynomial phase transform [27]. However, in the above methods, a temporal variation in the Doppler velocity within the CPI may reduce the time and velocity resolution, which constitutes a substantial problem.

One promising solution to the abovementioned problems is the weighted kernel density (WKD) estimation-based Doppler-velocity analysis [28]. In this method, the discrete range-$\tau$ points extracted from the range profile at each PRI are accurately converted to the associated Doppler velocity via the kernel-density-based probability density function estimator, which is a completely incoherent process. This method has a number of distinct advantages as follows.

1) There is no limitation on the Doppler-velocity resolution and the unambiguous velocity range, where the temporal resolution is determined by the PRI.
2) The connection problem of discrete range-$\tau$ points can be overcome by assessing the evaluation function using all of range-$\tau$ points with weighting function, namely, the batch processing can be achieved.
3) Each range-$\tau$ point and Doppler velocity holds one-to-one correspondence, which enables us to introduce an efficient data selection, regarding the radar image [29] or the Doppler velocity [30].

The key to the successful implementation of the WKD method is how accurately range-$\tau$ points can be extracted. The range resolution directly then determines the accuracy of the WKD method. To deal with human body responses, a reflection response obtained from each part of the human body must be decomposed. Since these responses are closely located, it is difficult to be decomposed using a traditional matched filter.

Manuscript received August 31, 2021; revised October 26, 2021 and January 17, 2022; accepted March 8, 2022. Date of publication March 11, 2022; date of current version April 4, 2022. This work was supported in part by JST, PRESTO under Grant JPMJPR1771, and in part by JST FOREST Program, Japan under Grant JPMJFR2025. *(Corresponding author: Shouhei Kidera.)*

Takeru Ando is with the Graduate School of Informatics and Engineering, The University of Electro-Communications, Tokyo 1828585, Japan (e-mail: ando.takeru@ems.cei.uec.ac.jp).

Shouhei Kidera is with the Graduate School of Informatics and Engineering, The University of Electro-Communications, Tokyo 1828585, Japan (e-mail: kidera@uec.ac.jp).

Digital Object Identifier 10.1109/JSTARS.2022.3158661

The original study in [28] introduced compressed sensing (CS), which is based on a superresolution technique or the Capon estimator [31], to obtain highly accurate results from the WKD processing. However, the above filtering schemes require both high computational cost and high SNR, making them unsuitable for use in realistic situations, and these issues have not been addressed in previous researches.

To overcome the above problems, a decomposition scheme integrating both the $k$-space and the Doppler-velocity space into the WKD framework is introduced in this article. While the original WKD is applicable to a single-input single-output (SISO) radar, there are innovative points to provide an extremely high range resolution performance by integrating data from multiple transmitters or receivers models, such as single-input multiple-output (SIMO) or multiple-input multiple-output (MIMO) models. In [32], it was demonstrated that the wavenumber space ($k$-space) decomposition (i.e., the decomposition in the direction-of-arrival (DOA) space) is capable of achieving high accuracy with low complexity in the range direction by applying the 2-D fast Fourier transform (2-D-FFT) to the 2-D array data, especially in high-frequency radar systems, such as the MMWs. This scheme was introduced in our previous study [33]. Additionally, the Doppler-velocity space decomposition is firstly incorporated into a $k$-space decomposition with the WKD scheme in this article. This can be achieved by employing the 4-D fast Fourier transform (4-D FFT) along with a 2-D array with a slow time $\tau$. Another innovative advantage of the proposed method over CS filtering is its significantly higher noise-robustness due to the use of a 4-D coherent integration and filtering process, as well as a massive reduction in the computational cost because of the use of the FFT process. Furthermore, because the Doppler velocity and wavenumbers are solely associated with the range-$\tau$ points, appropriate data selection can be achieved using a weighting function for the proximity in the Doppler and $k$-spaces using a unique feature of the WKD. Thus, the main contributions in this article are summarized as follows.

1) $k$- and Doppler velocity space decomposition further improve accuracy for range estimation, which also upgrades the Doppler velocity estimation in the WKD framework.
2) The 4-D FFT process could considerably reduce the computational complexity, compared to other filtering techniques.
3) Highly noise-robust feature is achieved via a coherent integration-based decomposition in $k$- and Doppler velocity space.

The numerical simulation results of two MMW radar models using 24 and 76 GHz bands and a 3-D simplified human model demonstrate that the proposed method provides a highly accurate Doppler-velocity profile at each pulse hit by simultaneously achieving high resolution features in terms of temporal, Doppler velocity, and range resolutions with considerably low complexity. Furthermore, the two experimental validations using the actual 24 GHz FMCW MIMO radar, assuming two metallic spheres with rotation and the real human walking motion, show that our proposed method retains the highest accuracy for range-Doppler extractions.

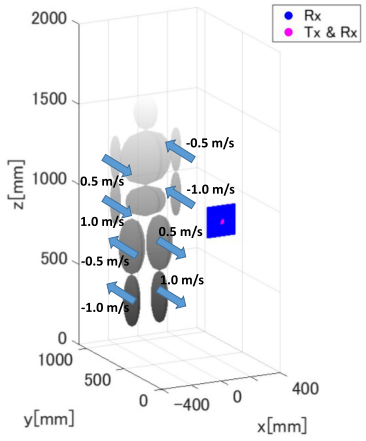


Fig. 1. Observation model.

## II. Observation Model

The observation model investigated in this article is shown in Fig. 1. Multiple transmitters (or single transmitter) and receivers constitute an array, which is placed on the $y = 0$ plane. A transmitter repeatedly transmits pulses with a fixed PRI, where the slow time $\tau$ is defined as the temporal PRI sequence. The transmitter and receiver locations are defined as $\boldsymbol{L}^{\mathrm{T}} = (x_T, 0, z_T)$ and $\boldsymbol{L}^{\mathrm{R}} = (x_R, 0, z_R)$, respectively. For each transmitter and receiver combination, the complex electric field is measured, which is defined as $s(\boldsymbol{L}^{\mathrm{T}}, \boldsymbol{L}^{\mathrm{R}}, R, \tau)$; $R = \mathrm{c}t/2$, where $t$ the fast time and c is the radio-wave speed. Then, the range extraction filter is applied to $s(\boldsymbol{L}^{\mathrm{T}}, \boldsymbol{L}^{\mathrm{R}}, R, \tau)$, and its response is defined as $\tilde{s}(\boldsymbol{L}^{\mathrm{T}}, \boldsymbol{L}^{\mathrm{R}}, R, \tau)$. Then, if we can measure a complex electric field as $\tilde{s}(\boldsymbol{L}^{\mathrm{T}}, \boldsymbol{L}^{\mathrm{R}}, R, \tau)$, either a pulse-Doppler radar or FMCW radar systems are applicable to the method presented in this study. A range-$\tau$ point is obtained by extracting the local maximum of $|\tilde{s}(\boldsymbol{L}^{\mathrm{T}}, \boldsymbol{L}^{\mathrm{R}}, R, \tau)|$ along the $R$ direction as

$$\frac{\partial |\tilde{s}(\boldsymbol{L}^{\mathrm{T}}, \boldsymbol{L}^{\mathrm{R}}, R, \tau)|}{\partial R} = 0 \tag{1}$$

$$|\tilde{s}(\boldsymbol{L}^{\mathrm{T}}, \boldsymbol{L}^{\mathrm{R}}, R, \tau)| \geq \alpha \max_{R,\tau} |\tilde{s}(\boldsymbol{L}^{\mathrm{T}}, \boldsymbol{L}^{\mathrm{R}}, R, \tau)| \tag{2}$$

where $\alpha$ denotes the threshold parameter and holds $0 \leq \alpha \leq 1$. Note that each range-$\tau$ point could express the distance $R$ to each reflection point on the target boundary, which is slow time $\tau$ variant.

## III. Doppler Velocity Analysis Method

### A. Original WKD

Many research studies on the micro-Doppler reflections obtained from the human motion have employed the time-Doppler frequency analysis using a coherent integration scheme such as the STFT, Wigner–Ville distribution, Radon transform, and Hough transform. However, they still have an inherent issue regarding the limitation in the temporal and frequency (Doppler velocity) resolutions, which are determined by the carrier wavelength and CPI. Moreover, when processing a quite high-range resolution output, such as ultra-wide band signals or responses

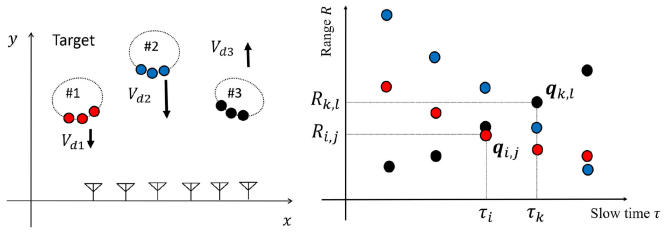


Fig. 2. Conceptual figure of the WKD method. Color solid circles in left and right figure denote scattering center points and range-$\tau$ points, respectively.

obtained from the Capon or CS filters, the RW effect also reduces the Doppler-velocity resolution, especially when dealing with a high-acceleration motion. The above problems can be resolved by the WKD method [28], where a group of discrete range-$\tau$ points defined in (2) can be converted to the corresponding Doppler velocity with a one-to-one correspondence using a completely incoherent process. The original WKD methodology is briefly described below.

In this method, a differential value between the focused and surrounding range-$\tau$ points denoted as $\boldsymbol{q}_{i,j}$ and $\boldsymbol{q}_{k,l}$, respectively. Here, in the definition of $\boldsymbol{q}_{i,j}$, the subscript $i$ presents the $i$th slow time snapshot at $\tau_i$, and the subscript $j$ express the index number of the extracted range-$\tau$ points at each $\tau_i$. Furthermore, this combination generates a possible Doppler velocity, which is defined as $v_{\rm d}(\boldsymbol{q}_{i,j}, \boldsymbol{q}_{k,l}) \equiv (R_{i,j} - R_{k,l})/(\tau_i - \tau_k)$. Using a number of these possible Doppler velocities, the optimal Doppler velocity of $\boldsymbol{q}_{i,j}$ can be calculated by maximizing the weighted Gaussian mixture-based kernel-density estimator as follows:

$$\hat{v}_{\rm d}(\boldsymbol{q}_{i,j}) = \arg\max_{v_{\rm d}} \sum_{k,l} \exp\left(-\frac{\left||\tilde{s}(\boldsymbol{q}_{i,j})| - |\tilde{s}(\boldsymbol{q}_{k,l})|\right|^2}{2\sigma_s^2}\right) \times \exp\left(-\frac{|\tau_i - \tau_k|^2}{2\sigma_\tau^2}\right) \exp\left(-\frac{|v_d - \tilde{v}_{\rm d}(\boldsymbol{q}_{i,j}, \boldsymbol{q}_{k,l})|^2}{2\sigma_{v_d}^2}\right) \quad (3)$$

where $|\tilde{s}(\boldsymbol{q}_{i,j})|$ is the signal strength of the filter response described in Section II, $\sigma_s$, $\sigma_\tau$, and $\sigma_{v_d}$ are constants, and their roles are detailed in [28]. Note that, these parameters can be determined by considering the assumed PRI or velocity variations. In particular, since $\sigma_\tau$ expresses a correlation length along a slow-time direction, it is set as a couple of PRIs. Additionally, $\sigma_{v_{\rm d}}$ is set to a smaller value than the assumed Doppler-velocity accuracy.

Fig. 2 shows a conceptual figure of the WKD method. To calculate the Doppler velocity for the focused range-$\tau$ point as $\boldsymbol{q}_{i,j}$, the WKD algorithm calculates the inclinations among all possible range-$\tau$ point $\boldsymbol{q}_{k,l}$, except itself, as $v_{\rm d}(\boldsymbol{q}_{i,j}, \boldsymbol{q}_{k,l})$. Note that, in calculating $v_{\rm d}(\boldsymbol{q}_{i,j}, \boldsymbol{q}_{k,l}) \equiv (R_{i,j} - R_{k,l})/(\tau_i - \tau_k)$ among multiple candidates of range-$\tau$ points, it requires tracking or connection preprocessing; however, the WKD method avoids this by introducing (3), where considers all possible combinations of discrete range-$\tau$ points, namely, the incoherent batch conversion from a range-$\tau$ point $\boldsymbol{q}_{i,j}$ to its associated Doppler velocity $v_{\rm d}(\boldsymbol{q}_{i,j})$ can be achieved. As a result, low computational

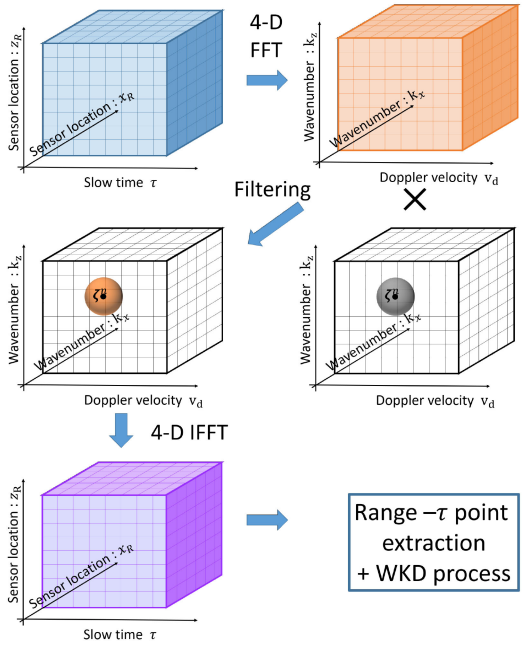


Fig. 3. Decomposition scheme of the Doppler velocity and $k$-space in the proposed method.

complexity, which is a significant advantage over other discrete-point-based approaches, can be achieved. Note that, the Doppler velocity $v_d(\boldsymbol{q}_{i,j})$ is determined at each instantaneous slow time $\tau_i$, i.e., the temporal resolution of the WKD method is identical to a single PRI. While the existing coherent integration *e.g.*, STFT and Radon-Fourier transforms, the Doppler velocity is calculated using phase rotation amount of the center frequency, the WKD only calculates an inclination between neighbouring range-$\tau$ points as $v_{\rm d}(\boldsymbol{q}_{i,j}$ at each slow time $\tau$. Therefore, the WKD can avoid phase ambiguities and there is no lower limit for Doppler velocity and temporal resolution as described in [28].

However, the estimation accuracy of the WKD method largely depends on that of the range-$\tau$ points and can be reduced when various reflections from multiple parts of the human body interfere within a range resolution. Additionally, a super-range resolution technique is required to attain the maximum performance of the WKD method. The original study in [28] introduced the CS pulse-decomposition approach. However, this approach exhibits high SNR and a high computational cost when solving high-dimensional optimization problems. Furthermore, while the original WKD can be used in the single transmitter and receiver model, there is significant potential to enhance resolutions or noise-robust by integrating multiple transmitters and receivers, however, no such study exists.

### B. Proposed WKD Method

*1) Range Extraction Method—Doppler and $k$-Space Decomposition:* As a low-complexity and high-range resolution technique, the WKD method employs the $k$-space and Doppler-velocity decomposition scheme using SIMO or MIMO model. The efficiency of the $k$-space decomposition was demonstrated in our previous study [32]. The proposed method is based on the

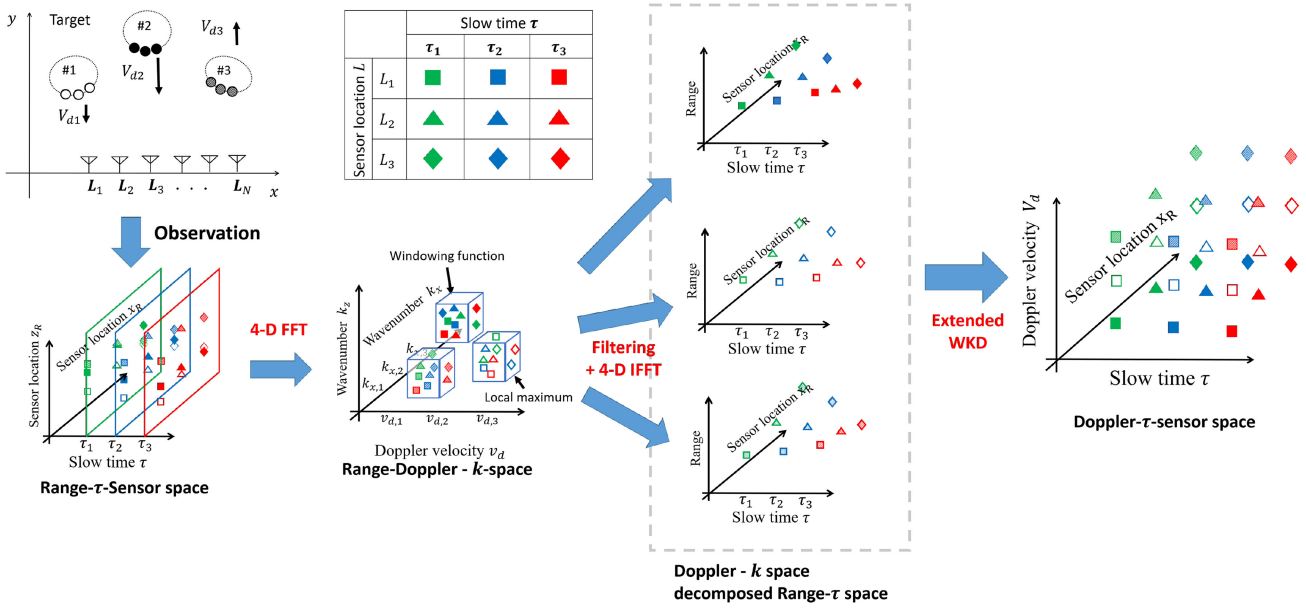


Fig. 4. Schematic diagram of the proposed data processing, where range-$\tau$ point associated with its wavenumber in the $k$-space is selectively processed by the WKD.

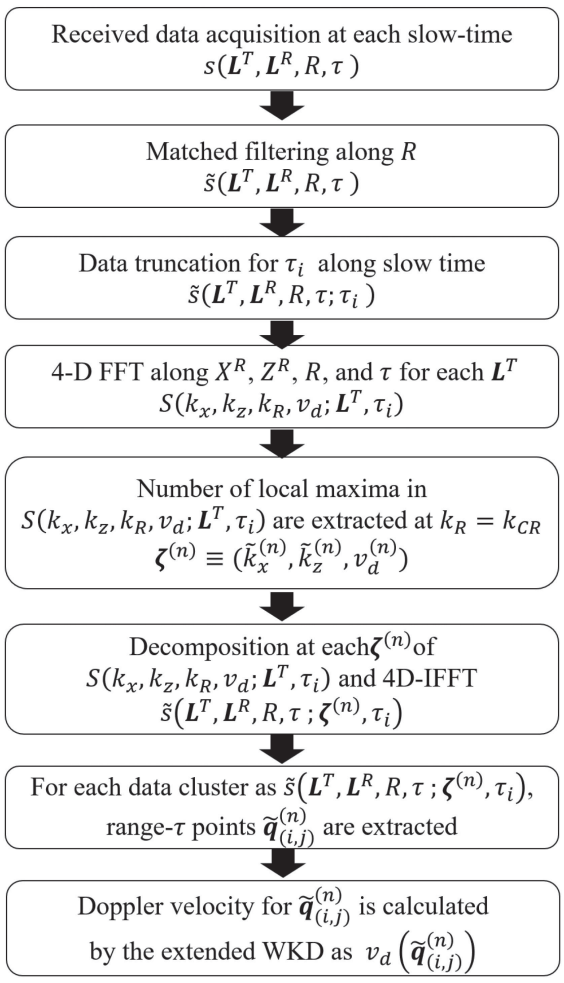


Fig. 5. Flowchart of the proposed method.

assumption that the reflection responses obtained from various parts of the human body not only have a different DOA, but also a different Doppler velocity, assuming motion. Then, the $k$-space decomposition contributes to the data separation along the DOA space, and the Doppler-velocity-space filtering enables us to decompose the data along different motion vectors. To achieve low complexity, this method exploits the 4-D Fourier transform. Fig. 3 shows the decomposition scheme in $k$ and Doppler velocity spaces. First, the observation data at each transmitter $\boldsymbol{L}^{\mathrm{T}}$ are converted to the Doppler and $k$-space using the 4-D Fourier transform as follows:

$$S(k_x, k_z, k_R, v_{\mathrm{d}}; \boldsymbol{L}^T) = \iint_A \int_T \int_{\mathcal{R}} \tilde{s}(\boldsymbol{L}^T, x_R, z_R, R, \tau) \times e^{-j(k_x x_R + k_z z_R + k_R R + \omega\tau)} dx_R dz_R dR d\tau \quad (4)$$

where $A$ denotes the aperture area, $k_R$ denotes the wavenumber (spatial frequency) of $R$, $k_x$, and $k_z$ are the wavenumbers of $x_R$ and $z_R$, respectively, which correspond to the azimuth and elevation angles. $v_{\mathrm{d}} = \omega\lambda/4\pi$ and $T$ denotes the coherent integration time. $T$ and $\mathcal{R}$ denote the integration period along $\tau$ and $R$, respectively. Here, we focus on the $k_x$-$k_z$-$v_{\mathrm{d}}$ data at a specific $k_R = k_{\mathrm{CR}}$ which corresponds to the center frequency of the transmitted pulse. The $k_x$-$k_z$-$v_{\mathrm{d}}$ associated discrete points denoted as $\boldsymbol{\zeta}^{(n)} \equiv (\tilde{k}_x^{(n)}, \tilde{k}_z^{(n)}, v_{\mathrm{d}}^{(n)})$ can be extracted from the local maxima of $S(k_x, k_z, k_{\mathrm{CR}}, v_{\mathrm{d}}; \boldsymbol{L}^T))$ as follows:

$$\left.\begin{aligned} \partial|S(k_x, k_z, k_{\mathrm{CR}}, v_{\mathrm{d}}; \boldsymbol{L}^T)|/\partial k_x = 0 \\ \partial|S(k_x, k_z, k_{\mathrm{CR}}, v_{\mathrm{d}}; \boldsymbol{L}^T)|/\partial k_z = 0 \\ \partial|S(k_x, k_z, k_{\mathrm{CR}}, v_{\mathrm{d}}; \boldsymbol{L}^T)|/\partial v_{\mathrm{d}} = 0 \end{aligned}\right\} \quad (5)$$

where $n$ denotes the index number of local maxima. It is expected that the data around a point $\boldsymbol{\zeta}^{(n)}$ will include only the response reflection obtained from the associated $k_x$ and $k_z$ (namely, the

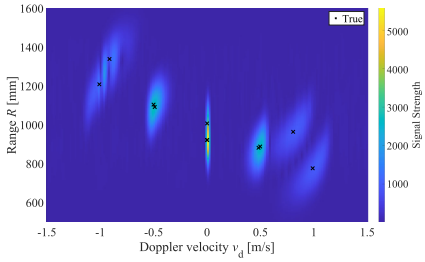


Fig. 6. Range-Doppler velocity profile using the STFT process, where the CPI is 0.4 s at SNR $= \infty$. Black dots denote the true Doppler velocities at $\tau = 0.2$ s.

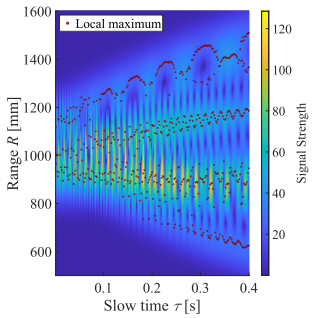


Fig. 7. Matched filter responses along slow-time at SNR $= \infty$. Red dots denote the local maximum, namely, range-$\tau$ points.

DOA) and the Doppler velocity $v_\mathrm{d}$. Then, each associated set of data is decomposed using the following filtering process and the 4-D inverse Fourier transform:

$$\tilde{s}(\boldsymbol{L}^T, \boldsymbol{L}^R, R, \tau; \boldsymbol{\zeta}^{(n)}) = \frac{1}{16\pi^4} \iiiint W(k_x, k_z, v_\mathrm{d}; \boldsymbol{\zeta}^{(n)}) S(k_x, k_z, k_R, v_\mathrm{d}; \boldsymbol{L}^T) \times e^{j(k_x x_R + k_z z_R + k_R R + \omega\tau)} dk_x dk_z dk_R d\omega. \quad (6)$$

Here, $W(k_x, k_z, v_\mathrm{d}; \boldsymbol{\zeta}^{(n)})$ denotes the windowing filter along $k_x$-$k_z$-$v_\mathrm{d}$ as the multi-dimensional Gaussian function, where filtering along $k_R$ is not applied, because the $S(k_x, k_z, k_R, v_\mathrm{d}; \boldsymbol{L}^T)$ has been already passed through the matched filter, i.e., the filtering was performed along $k_R$. The bandwidth of this windowing function should be set to a each resolution size of $k_x$, $k_z$, and $v_\mathrm{d}$. This bandwidth can be theoretically determined by the aperture size and CPI with the center wavelength. Finally, from the $n$th clustered decomposed data $\tilde{s}(\boldsymbol{L}^T, \boldsymbol{L}^R, R, \tau; \boldsymbol{\zeta}^{(n)})$, the range-$\tau$ points can be extracted from each cluster as $\tilde{\boldsymbol{q}}_{i,j}^{(n)} \equiv (\boldsymbol{L}_{i,j}^{\mathrm{T},(n)}, \boldsymbol{L}_{i,j}^{\mathrm{R},(n)}, R_{i,j}^{(n)}, \tau_i^{(n)})$ under the following condition:

$$\frac{\partial |\tilde{s}(\boldsymbol{L}^T, \boldsymbol{L}^R, R, \tau; \boldsymbol{\zeta}^{(n)})|}{\partial R} = 0 \quad (7)$$

$$|\tilde{s}(\boldsymbol{L}^T, \boldsymbol{L}^R, R, \tau; \boldsymbol{\zeta}^{(n)})| \geq \alpha \max_{R,\tau} |\tilde{s}(\boldsymbol{L}^T, \boldsymbol{L}^R, R, \tau; \boldsymbol{\zeta}^{(n)})| \quad (8)$$

where $\alpha$ denotes the threshold parameter and holds $0 \leq \alpha \leq 1$. Note that, the above decomposition process is achieved by the 4-D FFT and inverse FFT (IFFT) processes, which significantly reduce the total computational cost.

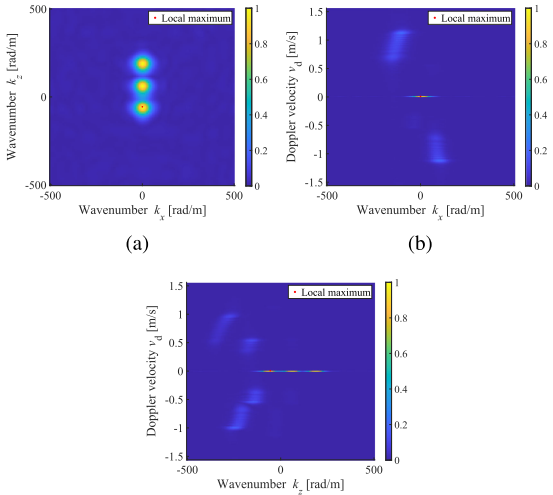


Fig. 8. Cross-sectional image of $k_x$-$k_z$-$v_\mathrm{d}$ spaces at SNR $= \infty$. Red dots denote local maximum points. (a) $v_\mathrm{d} = 0$ m/s. (b) $k_z = -56.0$ rad/m. (c) $k_x = 0$ rad/m.

*2) Extended WKD Method:* Fig. 4 shows the schematic process of Doppler k-space decomposition, assuming that the three separated targets are within the same range gate. By filtering the proximity area around three local maxima in Range-Doppler-$k$-space, the observation data are decomposed in $k$ and Doppler velocity spaces. The filtered data is then converted to each range-$\tau$ space using a 4-D IFFT process, where the Doppler velocity and $k$ values are associated. It should be noted that, although the range-$\tau$ points $\tilde{\boldsymbol{q}}_{i,j}^{(n)}$ can be divided into $n$ clusters as shown in Fig. 4, the number of range-$\tau$ points can be quite small, which incurs inaccuracy in the WKD process. We focus on the fact that the WKD process should be considered beyond a cluster. For this purpose, a new weight term was added to (3) corresponding to the $k$- and Doppler velocity spaces. The accuracy of the Doppler velocity estimation can be enhanced by selectively assessing the focused (for calculating $\hat{v}_\mathrm{d}(\tilde{\boldsymbol{q}}_{i,j}^{(n)})$) range-$\tau$ point $\tilde{\boldsymbol{q}}_{i,j}^{(n)}$ with the group of range-$\tau$ points $\tilde{\boldsymbol{q}}_{k,l}^{(m)}$, each of which has similar $k_x$, $k_z$, and $v_\mathrm{d}$. This scheme can be easily implemented using the following formula:

$$\hat{v}_\mathrm{d}(\tilde{\boldsymbol{q}}_{i,j}^{(n)}) = \arg\max_{v_\mathrm{d}} \sum_{k,l,m} \exp\left(-\frac{\left||\tilde{s}(\tilde{\boldsymbol{q}}_{i,j}^{(n)})| - |\tilde{s}(\tilde{\boldsymbol{q}}_{k,l}^{(m)})|\right|^2}{2\sigma_s^2}\right) \times \exp\left(-\frac{\left|\tau_i - \tau_k\right|^2}{2\sigma_\tau^2}\right) \exp\left(-\frac{\left|\left|\boldsymbol{k}^{(n)} - \boldsymbol{k}^{(m)}\right|\right|^2}{2\sigma_k^2}\right) \times \exp\left(-\frac{|v_\mathrm{d}^{(n)} - v_\mathrm{d}^{(m)}|^2}{2\sigma_{v_\mathrm{d,C}}^2}\right) \exp\left(-\frac{|v_d - \tilde{v}_\mathrm{d}(\tilde{\boldsymbol{q}}_{i,j}^{(n)}, \tilde{\boldsymbol{q}}_{k,l}^{(m)})|^2}{2\sigma_{v_d}^2}\right) \quad (9)$$

where $\boldsymbol{k}^{(n)} \equiv (\tilde{k}_x^{(n)}, \tilde{k}_z^{(n)})$. $\sigma_k$ and $\sigma_{v_\mathrm{d,C}}$ are the constant standard deviations of each Gaussian function. These values are generally determined by a couple of $k$- and Doppler velocity

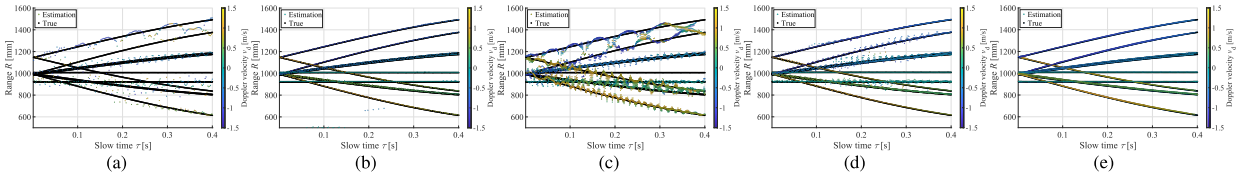


Fig. 9. Range-$\tau$ profile at the specific receiver point on (0, 0, 1000 mm) for each decomposition method at SNR $= \infty$. Black dots denote the true range-$\tau$ profiles. Color denotes the Doppler velocity. (a) Method I. (b) Method II. (c) Method III. (d) Method IV. (e) Method V.

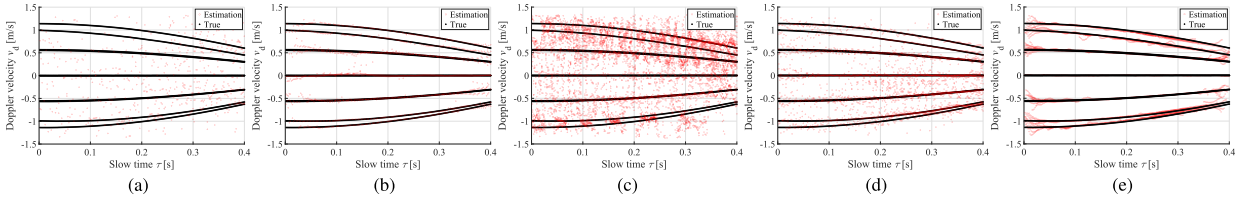


Fig. 10. Doppler-$\tau$ profile at the specific receiver point on (0, 0, 1000 mm) for each decomposition method at SNR $= \infty$. Black and red dots denote the actual and reconstruction Doppler velocities, respectively. (a) Method I. (b) Method II. (c) Method III. (d) Method IV. (e) Method V.

TABLE I
COMPARISON FOR COMPUTATIONAL TIMES PER ONE RECEIVER AND COMPLEXITY FOR EACH METHOD

| Method | Computational time | Computational complexity |
|---|---|---|
| Method I | 3.6 s | $O(N_R\ N_\tau\ N_X\ N_Y\ \log(N_R))$ |
| Method II | 508 s | $O(N_R^3\ N_\tau\ N_X\ N_Y)$ |
| Method III | 82.4 s | $O(N_R\ N_\tau\ N_X\ N_Y\ N_{\mathrm{v_d}}\ \log(N_\tau))$ |
| Method IV | 28.7 s | $O(N_R\ N_X\ N_Y\ N_\tau\ N_{\mathrm{k}}\ \log(N_X\ N_Y))$ |
| Method V | 133.7 s | $O(N_R\ N_X\ N_Y\ N_\tau\ N_{\mathrm{k-v_d}}\ \log(N_R\ N_X\ N_Y\ N_\tau))$ |

TABLE II
CUMULATIVE PROBABILITY OF SATISFYING EACH CRITERIA AT S/N $= \infty$

| | Number of points | $\mathrm{Err}_{v_\mathrm{d}} \leq 0.025$ m/s $\mathrm{Err}_R \leq 10$ mm | $\mathrm{Err}_{v_\mathrm{d}} \leq 0.025$ m/s $\mathrm{Err}_R \leq 50$ mm | $\mathrm{Err}_{v_\mathrm{d}} \leq 0.05$ m/s $\mathrm{Err}_R \leq 10$ mm | $\mathrm{Err}_{v_\mathrm{d}} \leq 0.05$ m/s $\mathrm{Err}_R \leq 50$ mm |
|---|---|---|---|---|---|
| Method I | 598 | 4.2 % | 9.7 % | 5.9 % | 18.1 % |
| Method II | 1594 | 78.9 % | 79.9 % | 91.0 % | 91.3 % |
| Method III | 7532 | 15.5 % | 20.0 % | 23.8 % | 32.2 % |
| Method IV | 3347 | 57.9 % | 59.1 % | 72.7 % | 73.8 % |
| Method V | 8648 | 82.5 % | 82.7 % | 94.7 % | 95.0 % |

resolutions, respectively, to achieve a correlation effect along the $k$ or $v_\mathrm{d}$ direction.

*3) Processing Chart of the Proposed Method:* Fig. 5 shows the flowchart of the proposed method, where more details are described as follows.

Step 1) Observation signals $s(\boldsymbol{L}^\mathrm{T}, \boldsymbol{L}^\mathrm{R}, R, \tau)$ are processed by the matched filter at each slow time $\tau$ denoted as $\tilde{s}(\boldsymbol{L}^\mathrm{T}, \boldsymbol{L}^\mathrm{R}, R, \tau)$.

Step 2) At a focused slow time $\tau_i$, $\tilde{s}(\boldsymbol{L}^\mathrm{T}, \boldsymbol{L}^\mathrm{R}, R, \tau)$ are windowed along the $\tau$ direction as $\tilde{s}(\boldsymbol{L}^\mathrm{T}, \boldsymbol{L}^\mathrm{R}, R, \tau; \tau_i)$ with a certain CPI denoted as $T$, where the center of windowing is set to $\tau_i$.

Step 3) $\tilde{s}(\boldsymbol{L}^\mathrm{T}, \boldsymbol{L}^\mathrm{R}, R, \tau; \tau_i)$ are converted to $S(k_x, k_z, k_R, v_\mathrm{d}; \boldsymbol{L}^T, \tau_i)$ via the 4-D FFT described in (4).

Step 4) Local maximum points $\boldsymbol{\zeta}^{(n)}$ are extracted from $S(k_x, k_z, k_R, v_\mathrm{d}; \boldsymbol{L}^T, \tau_i)$ in (5), and the filtering response $\tilde{s}(\boldsymbol{L}^T, \boldsymbol{L}^R, R, \tau; \boldsymbol{\zeta}^{(n)}, \tau_i)$ is obtained from (6).

Step 5) R-$\tau$ points $\tilde{\boldsymbol{q}}_{i,j}^{(n)}$ are extracted from the local maxima of $\tilde{s}(\boldsymbol{L}^T, \boldsymbol{L}^R, R, \tau; \boldsymbol{\zeta}^{(n)}, \tau_i)$ along $\tilde{R}$ in (8).

Step 6) For each range-$\tau$ point $\tilde{\boldsymbol{q}}_{i,j}^{(n)}$, the extended WKD method is applied in (9), and $\hat{v}_\mathrm{d}(\tilde{\boldsymbol{q}}_{i,j}^{(n)})$ is obtained.

Step 7) Each range-Doppler velocity point $\hat{v}_\mathrm{d}(\tilde{\boldsymbol{q}}_{i,j}^{(n)})$ is integrated over all clusters.

Step 8) $\tau_i$ is changed to $\tau_{i+1}$ and the Steps 2) to 6) are repeated.

Step 9) For all $\tau_i$, $\hat{v}_\mathrm{d}(\tilde{\boldsymbol{q}}_{i,j}^{(n)})$ is obtained.

## IV. NUMERICAL TESTS

### A. Numerical Setting

The numerical tests conducted using the simplified 3-D human walking model are described next. The human model was approximated by an aggregation of 11 ellipsoids, which represent the head, upper and lower arms, torso, and legs, with

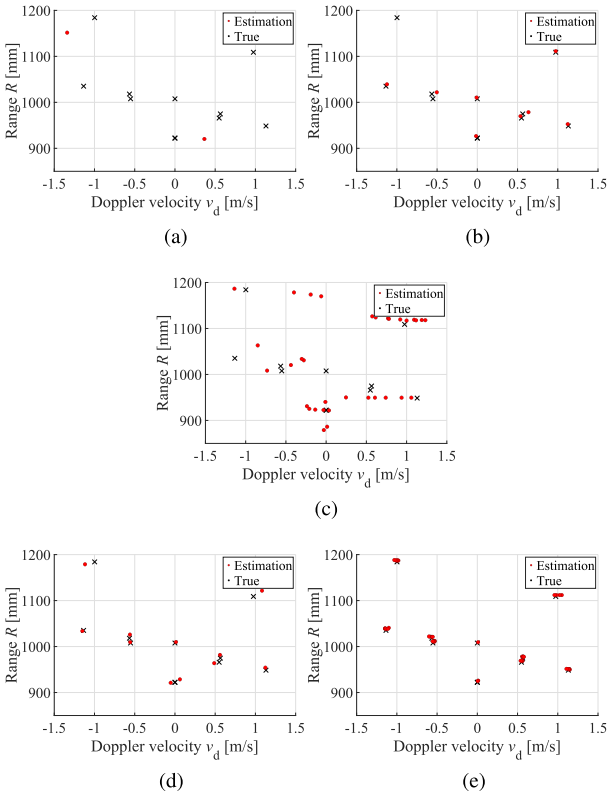


Fig. 11. Range-Doppler velocity profile at the specific receiver point on (0, 0, 1000 mm) and the slow time $\tau$=0.04 s at SNR $= \infty$. Black x and red dots denote the true and estimation points, respectively. (a) Method I. (b) Method II. (c) Method III. (d) Method IV. (e) Method V.

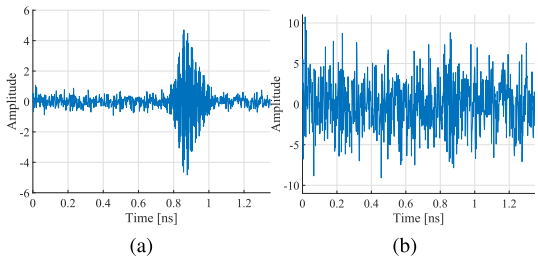


Fig. 12. Example of received signal at each SNR level. (a) SNR= 20 dB. (b) SNR= 0 dB.

each part of the body has a constant velocity linear motion along the $y$-axis as in Fig. 1. Although this model cannot accurately represent the actual human shape, it quantitatively assesses reconstruction performance in terms of range, Doppler velocity, and DOA, unlike the realistic human model described in [34]. For simplicity, high frequency microwave band of a 24-GHz center frequency and 0.5-GHz bandwidth was employed to produce the transmitting pulse. Since it is difficult to simulate the reflection data using an accurate electromagnetic forward solver, such as the finite difference time-domain solver, the data $s(\boldsymbol{L}^{\mathrm{T}}, \boldsymbol{L}^{\mathrm{R}}, R, \tau)$ were generated using the geometrical optics approximation in each pulse hit sequence [35], where interference among the objects is considered. An SIMO 2-D array was formed using one transmitter and a 31 $\times$ 31 receiver array in the $y = 0$ plane, where the spacing between the receivers was

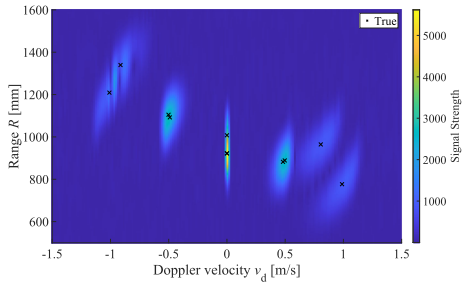


Fig. 13. Range-Doppler velocity profile using the STFT process at S/N $=$ 20 dB, where the CPI is 0.4 s. Black dots denote the true Doppler velocities at $\tau = 0.2$ s.

6.25 mm (corresponding to a half wavelength of the transmitted pulse) along both $x$- and $z$-axes. The SIMO scheme was selected instead of an MIMO system because it is suitable to actual scenarios in terms of fast data acquisition and cost. The aperture size in this case was 187.5 mm, and the angular resolution is 1.90 degrees in assuming that the distance from the array to target is 1000 mm. The transmitter was placed at the center of the array at $\boldsymbol{L}_T = (0, 0, 0)$. The PRI was set to 2 ms, and the number of pulse hits was 200, denoting a total observation time of 0.4 s. Under these settings, the theoretical resolution and the unambiguous range for the Doppler velocity are 0.0156 m/s (with 0.4 s CPI) and $\pm$1.5 m/s, respectively, according to the Fourier transform. Fig. 6 shows the STFT responses at the specific receiver points at (0, 0, 1000 mm) using all pulse hits, namely, its coherent integration period is 0.4 s. As shown in this figure, while the STFT offers a sufficient Doppler velocity resolution around the zero Doppler velocity, which corresponds to the static object, such as head, upper and lower torsos, responses around moving object, arm, leg, offer considerably blurry responses, and then, the instantaneous Doppler velocity at each slow time is hardly obtained in this profile. This is because the arm or leg has a variant Doppler velocity along slow time, and its response would move on range-Doppler profile, where its temporal information has been lost. Thus, the STFT or other coherent integration-based approach severely suffers from the tradeoff limitation of the temporal and Doppler velocity resolutions.

Fig. 7 shows the matched filter responses in the range-$\tau$ space of a specific receiver position at (0, 0, 1000 mm). Although 11 reflection responses (pulses) for each $\tau$ were expected, Fig. 7 shows that the traditional matched filter responses could not decompose each reflection, because a number of these reflection pulses were overlapped within a 300 mm range resolution. Fig. 8 shows cross-sectional images of the $k_x$, $k_z$, and $v_{\mathrm{d}}$ spaces, and distinguishable responses along different wavenumbers, namely, the DOA and Doppler velocities, corresponding to different parts of the human body can be observed in each space. To demonstrate the efficiency of the proposed method, which combines the $k$- and Doppler-velocity decomposition, five different methods were compared as follows.

Method I (Original WKD) refers to the original WKD method, which uses the range-$\tau$ points extracted from the matched filter response shown in 7.

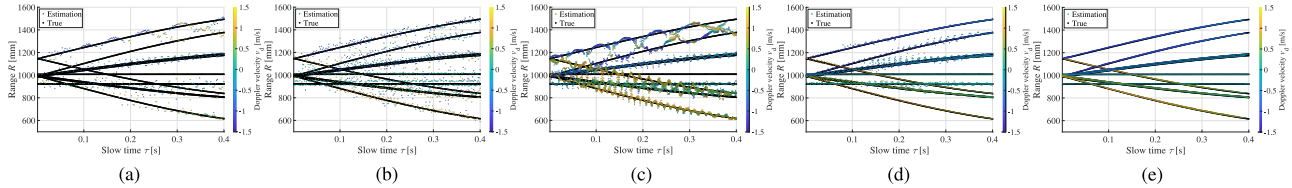


Fig. 14. Range-$\tau$ profile at the specific receiver point on (0, 0, 1000 mm) for each decomposition method at SNR $=$ 20 dB. Black dots denote the true range-$\tau$ profiles. Color denotes the Doppler velocity. (a) Method I. (b) Method II. (c) Method III. (d) Method IV. (e) Method V.

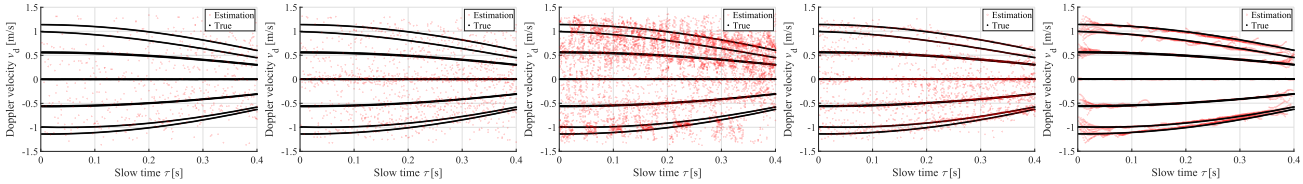


Fig. 15. Doppler-$\tau$ profile at the specific receiver point on (0, 0, 1000 mm) for each decomposition method at SNR $=$ 20 dB. Black and red dots denote the actual and reconstruction Doppler velocities, respectively. (a) Method I. (b) Method II. (c) Method III. (d) Method IV. (e) Method V.

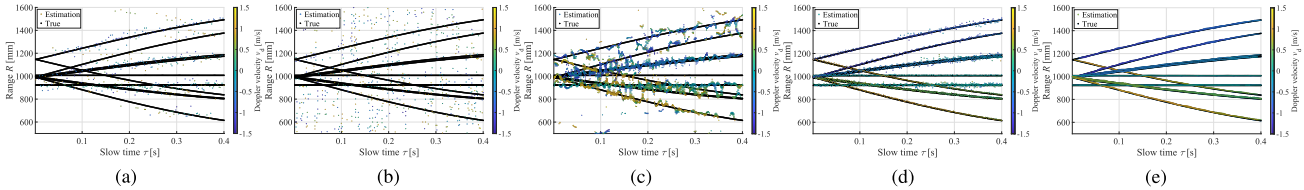


Fig. 16. Range-$\tau$ profile at the specific receiver point on (0, 0, 1000 mm) for each decomposition method at SNR $=$ 0 dB. Black dots denote the true range-$\tau$ profiles. Color denotes the Doppler velocity. (a) Method I. (b) Method II. (c) Method III. (d) Method IV. (e) Method V.

Method II (Original WKD+CS) employs the original WKD method, but uses a CS filter to extract the range-$\tau$ points [28].

Method III (WKD w/$v_{\mathrm{d}}$ Decomp.) is based on the Doppler-velocity decomposition scheme, where the 1-D FFT and IFFT with a filtering process in the Doppler-velocity space are applied to decompose the data. $(\sigma_{v_{\mathrm{d,C}}}, \sigma_k) = (0.02\ \mathrm{m/s}, \infty)$ in (9) is used.

Method IV (WKD w/$k$ Decomp.) employs the $k_x$ and $k_z$ space decomposition, namely, the 2-D FFT and IFFT, which are applied along $X$ and $Z$ with a filtering process [33]. $(\sigma_{v_{\mathrm{d,C}}}, \sigma_k) = (\infty, 7.0\ \mathrm{rad/m})$ in (9) is used.

Method V ($v_{\mathrm{d}} + k$ Decomp.) is the proposed method, namely, 3-D space filtering along the Doppler and $k$ spaces. $(\sigma_{v_{\mathrm{d,C}}}, \sigma_k) = (0.02\ \mathrm{m/s}, 7.0\ \mathrm{rad/m})$ in (9) is used.

Note that the parameters $(\sigma_s, \sigma_{\mathrm{v_d}}, \sigma_\tau) = (0.7, 0.2\ \mathrm{m/s}, 40\ \mathrm{ms})$ are used in all methods.

### B. Results in Noise-Free Case

First, the estimation results in the noise-free case are presented. The results of the range-$\tau$ points extracted using each of the abovementioned methods are shown in Fig. 9. Table I summarizes the corresponding computational time and complexities while using an Intel(R) Xeon(R) Silver 4210 @ 2.20 GHz processor with 1024-GB RAM. The computational complexity is expressed as the Randau notation as $O(*)$, where $N_{\mathrm{X}}$ and $N_{\mathrm{Z}}$ represent the numbers of 2-D FFT points along $x$- and $z$-axes, respectively. $N_{\mathrm{R}}$ and $N_\tau$ denote the numbers of samples along a fast and slow time, respectively. $N_{\mathrm{v_d}}$, $N_{\mathrm{k}}$, and $N_{\mathrm{k-v_d}}$ express the numbers of local maxima in the Doppler or k-space, used in Methods III, IV, and V (the proposed method), respectively. In general, $l_1$ norm minimization algorithm used in the CS filter, its complexity is estimated as $O(N_{\mathrm{R}}^3)$ [42]. In this case, $N_{\mathrm{X}} = 128$, $N_{\mathrm{Z}} = 128$, $N_{\mathrm{R}} = 700$, $N_\tau = 200$, $N_{\mathrm{v_d}} = 25$, $N_{\mathrm{k}} = 11$, and $N_{\mathrm{k-v_d}} = 55$. As shown in Fig. 9(a), the filtering process using a simple matched filter significantly suffers from inaccuracy in the range-$\tau$ point extraction due to the insufficient range resolution (300 mm), which cannot decompose the reflection responses obtained from each part of the human body. In addition, although Method II (namely, CS filtering) achieves an accurate and superresolution range extraction performance, it exhibits a quite large computational cost because the CS process is based on a high-dimensional optimization process for each slow time and sensor combination. Regarding Methods III and IV [Fig. 9(c) and (d), respectively], although the Doppler velocity and k-space decomposition schemes improve the accuracy of the range-$\tau$ points compared with that obtained from Method I, it still cannot

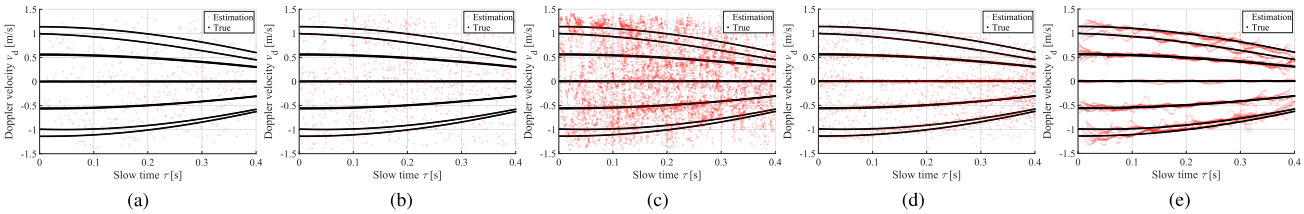


Fig. 17. Doppler-$\tau$ profile at the specific receiver point on (0, 0, 1000 mm) for each decomposition method at SNR = 0 dB. Black and red dots denote the actual and reconstruction Doppler velocities, respectively. (a) Method I. (b) Method II. (c) Method III. (d) Method IV. (e) Method V.

TABLE III
CUMULATIVE PROBABILITY OF SATISFYING EACH CRITERIA AT S/N = 20 DB

| | Number of points | $\mathrm{Err}_{v_\mathrm{d}} \leq 0.025$ m/s $\mathrm{Err}_R \leq 10$ mm | $\mathrm{Err}_{v_\mathrm{d}} \leq 0.025$ m/s $\mathrm{Err}_R \leq 50$ mm | $\mathrm{Err}_{v_\mathrm{d}} \leq 0.05$ m/s $\mathrm{Err}_R \leq 10$ mm | $\mathrm{Err}_{v_\mathrm{d}} \leq 0.05$ m/s $\mathrm{Err}_R \leq 50$ mm |
|---|---|---|---|---|---|
| Method I | 596 | 4.0% | 9.7 % | 6.2 % | 15.8 % |
| Method II | 1412 | 10.3 % | 18.3 % | 17.4 % | 31.5 % |
| Method III | 7215 | 12.5 % | 17.4 % | 20.4 % | 29.7 % |
| Method IV | 3331 | 57.8 % | 59.1 % | 71.8 % | 73.0 % |
| Method V | 8724 | 81.0 % | 81.3 % | 94.3 % | 94.5 % |

TABLE IV
CUMULATIVE PROBABILITY OF SATISFYING EACH CRITERIA AT S/N = 0 DB

| | Number of points | $\mathrm{Err}_{v_\mathrm{d}} \leq 0.025$ m/s $\mathrm{Err}_R \leq 10$ mm | $\mathrm{Err}_{v_\mathrm{d}} \leq 0.025$ m/s $\mathrm{Err}_R \leq 50$ mm | $\mathrm{Err}_{v_\mathrm{d}} \leq 0.05$ m/s $\mathrm{Err}_R \leq 10$ mm | $\mathrm{Err}_{v_\mathrm{d}} \leq 0.05$ m/s $\mathrm{Err}_R \leq 50$ mm |
|---|---|---|---|---|---|
| Method I | 453 | 1.6% | 4.4 % | 2.7 % | 9.7 % |
| Method II | 956 | 0.6 % | 2.4 % | 0.9 % | 3.8 % |
| Method III | 8955 | 6.0 % | 9.5 % | 11.5 % | 17.7 % |
| Method IV | 2685 | 44.8 % | 47.1 % | 62.1 % | 65.6 % |
| Method V | 8737 | 58.5 % | 59.7 % | 83.6 % | 84.5 % |

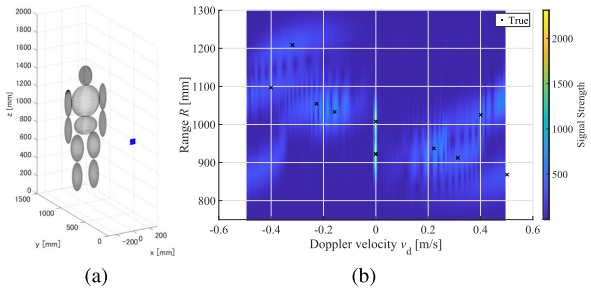


Fig. 18. (a) 76 GHz band SIMO observation model. Magenta and blue dots denote the transmitter and receivers, respectively. (b) Range-Doppler velocity profile using the STFT process, where the CPI is 0.4 s. Black dots denote the true Doppler velocities at $\tau = 0.2$ s.

provide sufficient accuracy due to lack of range resolution. In contrast, Method V (namely, the proposed method) achieves highly accurate and well decomposed range-$\tau$ point extraction performance with considerably lower complexity than that of Method II by avoiding the optimization process. Note that, although the CS process must be applied to each receiver, the proposed method simultaneously provides range-$\tau$ point extraction to all receivers using the 4-D FFT process.

Furthermore, Fig. 10 shows the results of the Doppler velocity estimations. It also demonstrates that the proposed method exhibits the highest accuracy due to highly accurate range-$\tau$ point extraction feature. To be more clear for an effectiveness, Fig. 11 show an example of the Doppler-velocity and range profiles, at a specific slow time and the receiver, and demonstrates that the Methods I, II, and III could not provide a sufficient number of range-Doppler points, due to insufficient resolution along range axis. While the Method IV relatively increases accurately reconstructed range-Doppler samples, there are a few missing samples or inaccurate estimation. On the contrary, the proposed method, namely, Method V provided all necessary range-Doppler points with high accuracy, and it also demonstrates that the decomposition in both Doppler and $k$ spaces are indispensable to offer an accurate range Doppler velocity profile, in such much interfered situation. Table II shows the quantitative error analysis, where the cumulative probabilities that satisfy different error criteria regarding the Doppler velocity and range are investigated. First, this table shows that the Method II using the CS filter offers a high probability of $\leq 78\%$ in most strict criteria, as $\mathrm{Err}_{v_\mathrm{d}} \leq 0.025$ m/s $\mathrm{Err}_R \leq 50$ mm, which is consistent with the results shown in Figs. 9 and 10. This table also shows that the proposed method retains the highest cumulative probability for all error criteria. Note that over 90 % range-$\tau$ points within a 0.05 m/s Doppler velocity (i.e, the 2.7 times of theoretical Doppler resolution) and 10 mm range (i.e., 1/30 of theoretical range resolution), can be simultaneously achieved at each slow-time. This means that its temporal resolution is equivalent to a single PRI, which cannot be provided

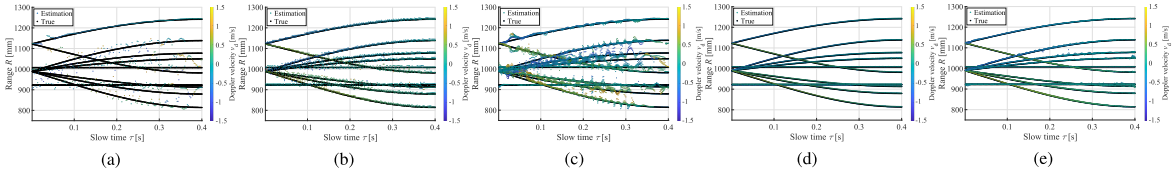


Fig. 19. Range-$\tau$ profile at the specific receiver point on (0, 0, 1000 mm) for each decomposition method in 76 GHz band model and time-variant motion model. Black dots denote the true range-$\tau$ profiles. Color denotes the Doppler velocity. (a) Method I. (b) Method II. (c) Method III. (d) Method IV. (e) Method V.

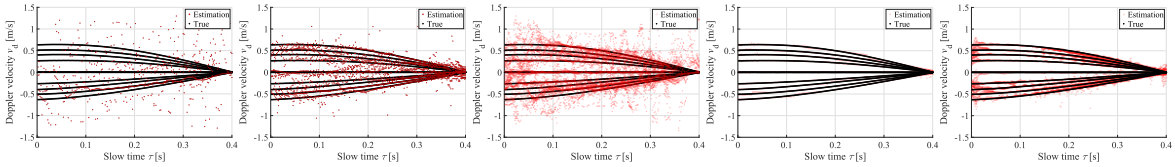


Fig. 20. Doppler-$\tau$ profile at the specific receiver point on (0, 0, 1000 mm) for each decomposition method in 76 GHz band model and time-variant motion model. Black and red dots denote the actual and reconstruction Doppler velocities, respectively. (a) Method I. (b) Method II. (c) Method III. (d) Method IV. (e) Method V.

TABLE V
CUMULATIVE PROBABILITY OF SATISFYING EACH CRITERIA IN THE 76 GHZ BAND RADAR WITH TIME-VARIANT VELOCITY MODEL

| | Number of points | $\mathrm{Err}_{v_{\mathrm{d}}} \leq 0.20$ m/s $\mathrm{Err}_R \leq 50$ mm | $\mathrm{Err}_{v_{\mathrm{d}}} \leq 0.20$ m/s $\mathrm{Err}_R \leq 100$ mm | $\mathrm{Err}_{v_{\mathrm{d}}} \leq 0.50$ m/s $\mathrm{Err}_R \leq 50$ mm | $\mathrm{Err}_{v_{\mathrm{d}}} \leq 0.50$ m/s $\mathrm{Err}_R \leq 100$ mm |
|---|---|---|---|---|---|
| Method I | 684 | 20.3 % | 25.6 % | 31.0 % | 38.7 % |
| Method II | 2539 | 47.6 % | 52.2 % | 67.0 % | 72.6 % |
| Method III | 12686 | 38.3 % | 41.3 % | 55.1 % | 60.7 % |
| Method IV | 2194 | 95.7 % | 95.8 % | 99.8 % | 99.8 % |
| Method V | 20793 | 84.4 % | 85.0 % | 95.6 % | 95.9 % |

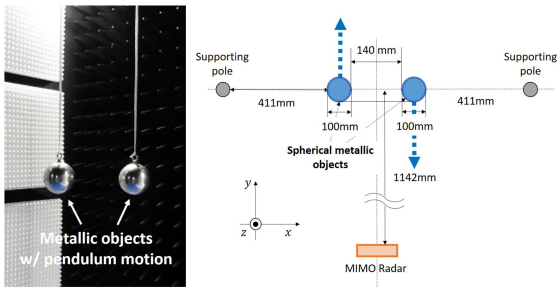


Fig. 21. Experimental scene and geometry for two spherical objects with pendulum motions.

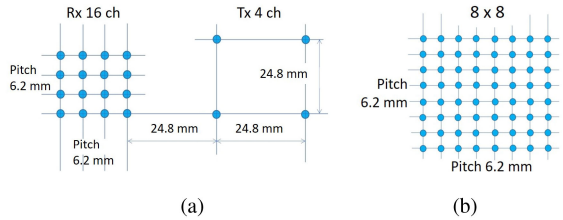


Fig. 22. Real and virtual configurations of MIMO radar with 4 transmitters and 16 receivers in the experiment.

by other coherent integration-based Doppler velocity methods, due to the uncertainty principle. Also note that, although the proposed method employs a coherent integration scheme along the 2-D array and a slow time to decompose the data, the Doppler velocity estimator in the WKD is an incoherent process. The above features are available, even in the case a lower limitation in the angular or velocity determined by the Fourier transform is beyond the actual target arrangement or motion velocity.

### C. Results in the Presence of Noise

Next, a noise-robust feature for each method is investigated. Here, Gaussian white noise is directly added to the received signal $s(\boldsymbol{L}^{\mathrm{T}}, \boldsymbol{L}^{\mathrm{R}}, R, \tau)$, where the SNR is defined as the ratio of the maximum signal power to the noise average power in the time domain. At first, SNR $= 20$ dB is assumed, which would be available in assuming a short-range sensing scenario, such as in [28]. Fig. 12 shows the examples of reflection responses at SNR $= 20$ and 0 dB cases, denoting that a signal is significantly contaminated by random noise. Fig. 13 shows the range-Doppler velocity profile obtained by the STFT approach, where the CPI or other parameters are set to the same in the case in Fig. 6. As shown in this figure, the STFT maintains the significant responses at each Doppler velocity or range, which is brought by coherent integration process, that is the one of most important advantages from the WKD based method. Furthermore, Figs. 14 and 15 show the range-$\tau$ point and Doppler-$\tau$ point profiles

TABLE VI
CUMULATIVE PROBABILITY OF SATISFYING EACH CRITERIA IN THE EXPERIMENTAL TEST. CASE OF TWO SPHERICAL TARGETS

| | Number of points | $\mathrm{Err}_{v_\mathrm{d}} \leq 0.20$ m/s $\mathrm{Err}_R \leq 50$ mm | $\mathrm{Err}_{v_\mathrm{d}} \leq 0.20$ m/s $\mathrm{Err}_R \leq 100$ mm | $\mathrm{Err}_{v_\mathrm{d}} \leq 0.50$ m/s $\mathrm{Err}_R \leq 50$ mm | $\mathrm{Err}_{v_\mathrm{d}} \leq 0.50$ m/s $\mathrm{Err}_R \leq 100$ mm |
|---|---|---|---|---|---|
| Method I | 226 | 50.0 % | 50.4 % | 67.7 % | 69.5 % |
| Method II | 235 | 26.4 % | 31.1 % | 41.3 % | 51.9 % |
| Method III | 4067 | 36.3 % | 36.5 % | 64.3 % | 66.1 % |
| Method IV | 819 | 40.8 % | 41.0 % | 69.6 % | 70.3 % |
| Method V | 3950 | 73.0 % | 73.3 % | 94.8 % | 95.4 % |

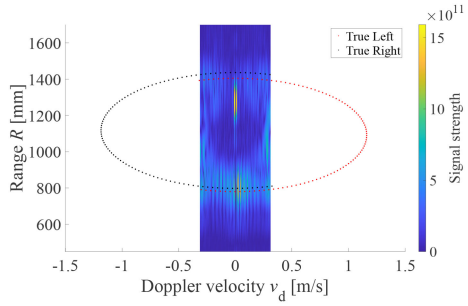


(a)

Fig. 23. Range-Doppler velocity profile using the STFT process in the experimental test using two spherical targets, where the CPI is 1.0 s. Black and red dots denote the actual Doppler velocity orbits of right and left spheres, respectively, among CPI duration. (a) STFT.

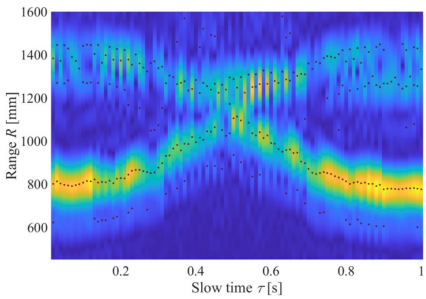


Fig. 24. Matched filter responses along slow-time in the experiment using two spherical targets. Red dots denote the lrange-$\tau$ points.

obtained from each method in this case. A quantitative error analysis is also shown in Table III. As shown in these results through Figs. 14, 15, and Table III, while the CS based range-$\tau$ extraction severely suffers from inaccuracy due to noise component, the proposed method (Method V) or other coherent integration-based decomposition (Methods III or IV) could maintain its range-$\tau$ points extraction performance, even compared with those obtained in noise-free case. Although the WKD approach does not exploit a coherent integration-based noise reduction, the coherent filtering process along the $k$ and $v_\mathrm{d}$ spaces significantly suppresses the noisy component, which could compensates the inherent disadvantage of the WKD method. Consequently, the proposed method has a significant advantage regarding noise reduction and simultaneously holds the unique features of the WKD method, i.e., it has no limitation on the resolution and the unambiguous range of the Doppler velocity and exhibits high temporal resolution being identical to the PRI.

For a noisier case, the case in SNR $= 0$ dB, is tested as follows. Figs. 16 and 17 show the range-$\tau$ point and Doppler-$\tau$ point profiles in each method, at the SNR of 0 dB, and Table IV also summarizes the results of the quantitative errors. Even, in such much lower SNR scenario, the proposed method retains its reconstruction accuracy in range and Doppler velocity, this is because the 4-D FFT-based coherent integration and its filtering scheme significantly suppress the noise components, resulting in the best applicability to realistic scenarios.

## V. APPLICABILITY TO 76 GHZ BAND WITH TIME-VARIANT MOTION

### A. Numerical Setting and Target Model

To validate the proposed method in a more promising and available frequency band, numerical tests using 76 GHz millimeter band are introduced, because these frequency bands become mainstream for practical MMW radar applications, such an automotive radar or other short range sensing sensors [36]–[41]. As in a typical 76 GHz band, transmitted pulse forms a 76 GHz center frequency with 1.0 GHz bandwidth, implying a range resolution of 150 mm. The GO is used to generate reflection data. Fig. 18(a) shows the observation model, which is similar to the previous model using a 2-D SIMO array with one transmitter and 31 $\times$ 31 receiver array in the $y = 0$ plane. In this case, the array spacing is 2 mm along the $x$-and $z$-axes, and the aperture size was 60 mm. That is the cross-range resolution is 32.9 mm at a distance of 1000 mm from the array to the target. The PRI, number of pulse hits, and total observation time are the same as in Section IV-A. However, the theoretical resolution and unambiguous range for the Doppler velocity are changed to $4.9 \times 10^{-3}$ m/s (with 0.4 s CPI) and $\pm$ 0.493 m/s, respectively. Furthermore, while each part of the human body is approximated by the same ellipsoid, each motion is presented by a time-variant model. The velocity of each motion is expressed as $v = \frac{2\pi A_i}{T_i} \cos(2\pi t/T_i)$, that is a time-derivative of a sinusoidal function, where $A_i$ and $T_i$ represents the amplitude and period of the sinusoidal curve for the $i$th part of the human body. In this case, $T_i = 1.6$ s in all parts, and $A_i = 0.62$ m/s for lower leg, $A_i = 0.30$ m/s for upper leg, $A_i = 0.60$ m/s for lower arm, and $A_i = 0.30$ m/s for upper arm are set.

### B. Results and Discussions

Fig. 18(b) shows the STFT responses at specific receiver points at (0, 0, 1000 mm), where the CPI is 0.4 s, indicating that the STFT responses could not express the actual time-variant Doppler velocity in such longer CPI, whereas the velocity

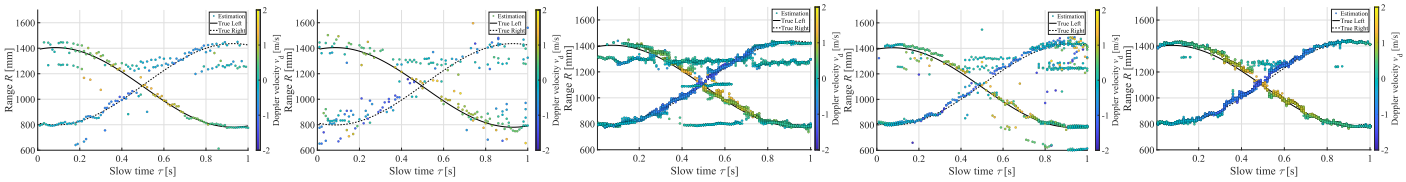


Fig. 25. Range-$\tau$ profile at the specific transmitter and receiver combination in experimental test using two spherical targets. Color denotes the Doppler velocity. (a) Method I. (b) Method II. (c) Method III. (d) Method IV. (e) Method V.

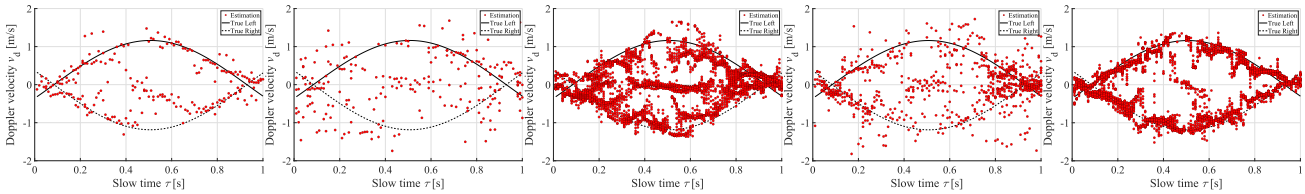


Fig. 26. Doppler-$\tau$ profile at the specific transmitter and receiver combination in experimental test using two spherical targets. Black and red dots denote the actual and reconstruction Doppler velocities, respectively. (a) Method I. (b) Method II. (c) Method III. (d) Method IV. (e) Method V.

TABLE VII
CUMULATIVE PROBABILITY OF SATISFYING EACH CRITERIA IN THE EXPERIMENTAL TEST: CASE OF REAL HUMAN WALKING MOTION

| | Number of points | $\mathrm{Err}_{v_\mathrm{d}} \leq 0.10$ m/s $\mathrm{Err}_R \leq 50$ mm | $\mathrm{Err}_{v_\mathrm{d}} \leq 0.10$ m/s $\mathrm{Err}_R \leq 100$ mm | $\mathrm{Err}_{v_\mathrm{d}} \leq 0.20$ m/s $\mathrm{Err}_R \leq 50$ mm | $\mathrm{Err}_{v_\mathrm{d}} \leq 0.20$ m/s $\mathrm{Err}_R \leq 100$ mm |
|---|---|---|---|---|---|
| Method I | 685 | 20.2 % | 28.6 % | 34.0 % | 46.3 % |
| Method II | 1112 | 15.0 % | 21.0 % | 22.0 % | 31.4 % |
| Method III | 39177 | 24.5 % | 35.5 % | 42.6 % | 58.1 % |
| Method IV | 4488 | 35.6 % | 41.9 % | 52.4 % | 60.4 % |
| Method V | 50378 | 43.9 % | 51.5 % | 64.5 % | 74.4 % |

resolution could be improved using a higher frequency model. Figs. 19 and 20 show the range-$\tau$ and the Doppler-velocity-$\tau$ profiles, respectively. The cumulative probability in each error criterion is shown in Table V. As shown in these figures and table, Methods I and III suffer from significant inaccuracy, indicating that Method III, such as the Doppler-velocity decomposition, is insufficient to decompose the range data even when using a higher frequency. Method II, as the original WKD+CS, offers a certain level of accuracy, but, it suffers from inaccuracy at lower SNR. Furthermore, Methods IV and V retain the most accurate profiles, demonstrating that in higher frequency and time-variant motion cases, the $k$-space decomposition is more effective because there would not be ambiguous responses under Nyquist condition sensor sampling, or it could achieve sufficient resolution in $k_x$ and $k_z$ space.

## VI. EXPERIMENTAL TEST

### A. Experimental Setting

To validate the proposed method in the real world, we conducted the following experiments. Fig. 21 shows the measurement setup used in the anechoic chamber, including the radar equipment and the two metallic spherical objects with a pendulum motion. We used FMCW and MIMO radar produced by a Sakura Tech Corp, which has a 24.15-GHz center frequency and a 2.0-GHz bandwidth, allowing us to achieve 75 mm range resolution. This MIMO radar has four transmitters and 16 receivers with planar patch antennas arranged on the plane ($y = 0$ mm), as shown in Fig. 22, which has 117 and 105 mm dimensions along the horizontal and vertical axes, respectively. Each patch antenna has a $\pm 13^\circ$ beamwidth in the horizontal and vertical directions, where its output power is 13 dBm. By considering the $8 \times 8$ virtual array arrangement [see Fig. 22(b)], the azimuth and elevation angular resolutions are both $4.1^\circ$, respectively. In the FMCW sequence, the sampling interval of the slow-time $\tau$ was set to 10 ms sweep interval corresponding to PRI. The observation time is 1.0 s and the total number of pulse hits is 100.

### B. Case of Rotating Two Metallic Spheres

We set two metallic spheres with 50 mm radius and 140 mm separation, both of which are suspended from a hanger rack with 411 mm separation. These two spheres have pendulum motions with 300 mm amplitude and 1.0 s period, along opposite sides of each other, implying that their motion vectors and DOA angles are different. The distance from the center of the pendulum motion to the MIMO radar is 1142 mm.

First, Fig. 23 shows the STFT responses using all the CPI as 1.0 s, with the theoretical Doppler resolution is $6.21 \times 10^{-3}$ m/s,

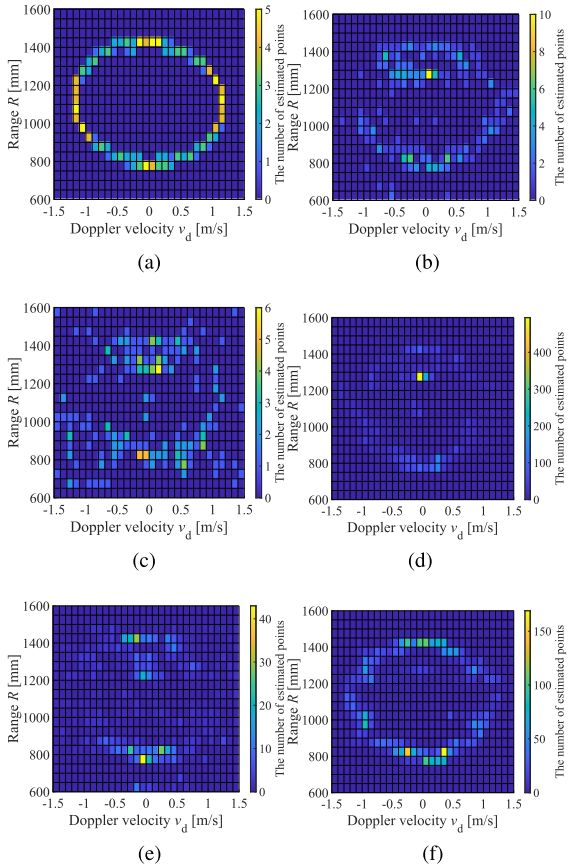


Fig. 27. Two-dimensional histograms on range-Doppler velocity space in the experimental test using two spherical targets. Color denotes the number of estimated points. (a) Theoretical. (b) Method I. (c) Method II. (d) Method III. (e) Method IV. (f) Method V.

and the unambiguous velocity range is $\pm$ 0.310 m/s. As shown in Fig. 23, the STFT could not cover the maximum velocity range for each object above $\pm$ 1.0 m/s, and the longer CPI could not express the actual Doppler velocity variance indicating that the temporal resolution is critically limited. Fig. 24 shows the matched filter responses in the range-$\tau$ space, and there are severe interfered responses around $0.4\,\mathrm{s} \leq \tau \leq 0.6\,\mathrm{s}$ due to the multiple reflections from both objects with the same range gate. Here, the average SNR is approximately 33 dB. The traditional matched filter process could not provide sufficiently accurate range-$\tau$ profile with a range resolution as 75 mm.

Figs. 25 and 26 show the range-$\tau$ and the Doppler-velocity-$\tau$ profiles using each method, respectively. As shown in these figures, while Methods I–IV could not offer an accurate Doppler-$\tau$ profile, the proposed method, as Method V, could retain a reliable Doppler velocity profile. Although the unambiguous range of the FFT based Doppler velocity conversion is narrower than that of actual velocity, the Doppler velocity decomposition is still effective in separating the data along with different Doppler velocities. Fig. 27 shows 2-D profiles of the histograms in range-Doppler space, and it demonstrated that our proposed method accurately reconstructs the actual trajectory of two pendulum motions. For $0.4\,\mathrm{s} \leq \tau \leq 0.6\,\mathrm{s}$, the $v_d$ decomposition plays a significant role in separating the reflections from two spheres at

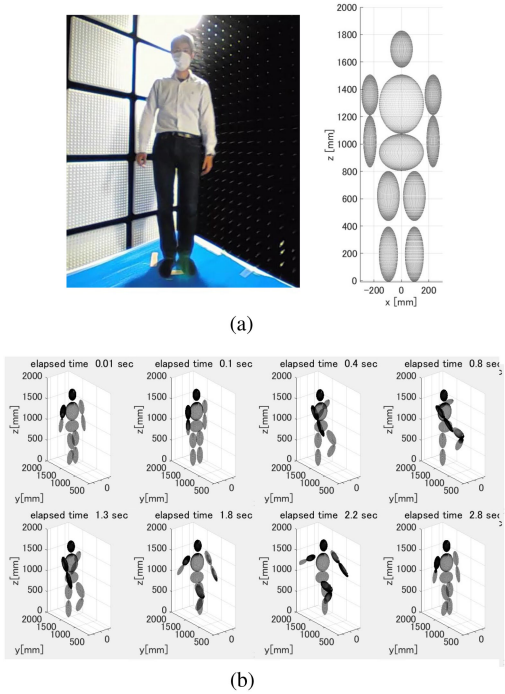


Fig. 28. Experimental scene and human walking numerical model in each elapsed time. (a) Photo and numerical model. (b) Numerical human model in each elapsed time.

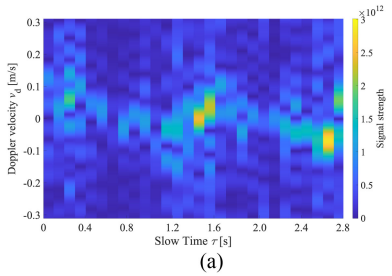


Fig. 29. Doppler velocity- $\tau$ profile using the STFT process in the real human walking model, where the CPI is 0.1 s. (a) STFT.

the same range gate. However, the $k$-space decomposition could suppress the unnecessary responses around $R = 1100$ mm from static hanger racks, which are located on both sides of the two spheres as in Fig. 21(b). Finally, Table VI show quantitative error analysis using the cumulative probability satisfying each error criteria, and this table provides the quantitative reliability of the proposed method's effectiveness, that is around 95% of data points satisfy the error criteria, $\mathrm{Err}_{v_\mathrm{d}} \leq 0.50$ m/s and $\mathrm{Err}_R \leq 50$ mm, where the theoretical range and Doppler velocity resolutions are 75 mm and $6.21 \times 10^{-3}$ m/s, respectively. These results show that the effectiveness of the proposed method was is demonstrated in a real world scenario using actual MMW radar equipment.

### C. *Case of Real Human Walking Motion*

To validate our proposed method in a more complicated or realistic scenario, the case of a real human body with stepping

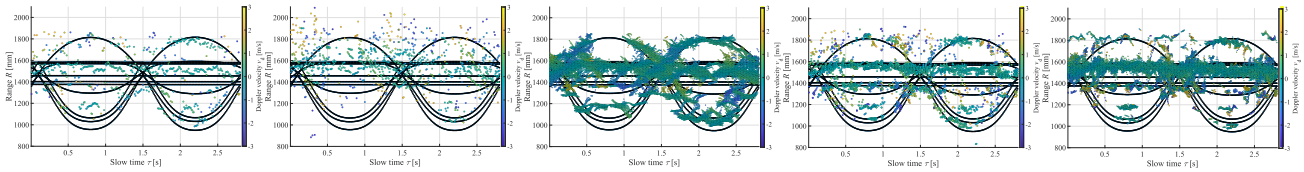


Fig. 30. Range-$\tau$ profile at the specific transmitter and receiver combination in experimental test with human walking motion. Black dots denote the ground truth (numerically approximated) range-$\tau$ profiles. Color denotes the Doppler velocity. (a) Method I. (b) Method II. (c) Method III. (d) Method IV. (e) Method V.

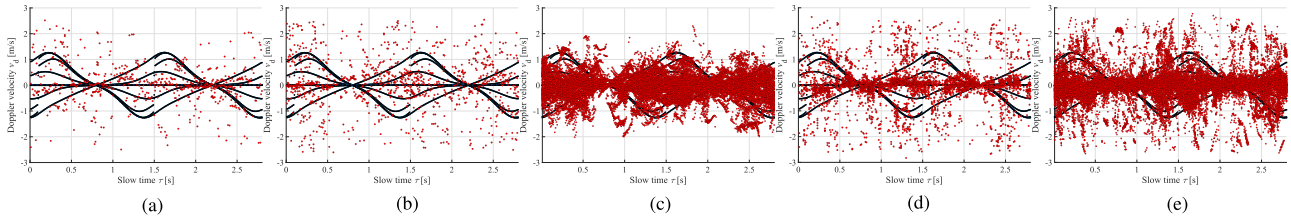


Fig. 31. Doppler-$\tau$ profile at the specific transmitter and receiver combination in experimental test with human walking motion. Black and red dots denote the ground truth (numerically approximated) and reconstruction Doppler velocity- $\tau$ profiles, respectively. (a) Method I. (b) Method II. (c) Method III. (d) Method IV. (e) Method V.

walking motion is investigated as follows. To provide a quantitative analysis for the obtained results, in terms of range-Doppler profiles, each moving part of the human body, such as arm and leg, is modeled using a simplified mathematical model based on actual human walking. Fig. 28 shows the experimental setup for real human body in walking motion, and the numerical walking model, which would be accurately fitted in a realistic walking motion in the maximum extent at each elapsed time. The same radar unit and parameters such as PRI, are used in the description of Section VI-A. Thus, the unambiguous velocity range is $\pm$ 0.310 m/s and it is significantly lower than the maximum velocity of the arm or leg in the walking motion, which is over $\pm 1.0$ m/s. During the measurement, the human has a foot-to-foot motion in the same position, which is approximately 1500 mm away from the radar site.

First, Fig. 29 shows the Doppler-$\tau$ profile generated by the STFT results, where the CPI is set to 0.10 s and $R = 1507$ mm is fixed. As shown in this figure, while we were able to recognize some time-variance responses of Doppler velocity, the STFT was unable to cover the maximum velocity range of a human walking motion, resulting in a velocity aliasing effect. Figs. 30 and 31 show the range-$\tau$ and Doppler-velocity-$\tau$ profiles for each method. In addition, Table VI summarizes the comparison of the cumulative probability satisfying each error criterion. This quantitative comparison demonstrates that while Method I or III, could not resolve the range profiles due to a lack of range resolution, the cumulative probability for each error criterion is significantly lower than other approaches. Note that, Method II, the CS filter, considerably suffers from inaccuracy due to a lower level of SNR, as discussed in Section IV-C. However, Method IV or V (the proposed method) retains a certain level of accuracy for the range and Doppler velocity calculations, even in such complicated situations, due to k-space or Doppler decomposition. Since the ground truth curve could not necessarily represent the actual orbit of range and Doppler velocity, the above quantitative comparison should be treated carefully. Furthermore, since the actual human body is not expressed as discrete objects aggregations, but continuous or distributed objects, the ground truth range or velocity -$\tau$ profile, is rarely available, and the accuracies in each method would be worse than those in discrete target cases as described in Section VI-B. Future studies should provide more discussions and investigations on the above real human walking motion issues.

## VII. Conclusion

This article focuses on a highly accurate range and Doppler-velocity decomposition method regarding the WKD-based Doppler-velocity estimator, assuming an MMW short-range sensing scenario for human body recognition. Since there are severe bandwidth limitations in generic MMW radars, such as the IS band, the decomposition of each reflection response obtained from a part of the human body is critically challenging. To overcome this difficulty, both the Doppler velocity and $k$-space decomposition were introduced in the WKD method to provide unlimited resolution and the unambiguous range in the Doppler velocity with a single PRI temporal resolution. Assuming a human walking scenario, each reflection response can be decomposed into a different Doppler velocity and $k$-space (namely, the DOA space). Then, by applying a filtering process in these spaces, highly accurate range-$\tau$ extraction and high noise reduction can be achieved due to the 4-D Fourier-transform integration scheme. The numerical simulation of a simplified human model using a 24-GHz center frequency with a 0.5-GHz bandwidth radar demonstrated that the proposed method achieves quite accurate range and Doppler-velocity profiles, which cannot be achieved by other decomposition processes in the Doppler velocity and $k$-space. A notable advantage of this method, since the decomposition is performed using the 4-D FFT and IFFT process, it significantly reduces computational complexity compared with that required by the

CS-filter-based method adopted in [28]. Although the proposed method is applied to human body recognition, it can also be applied to other target models, where a number of discrete scatterers are included in the nominal range, Doppler velocity, and angular resolution.

Furthermore, while this study assumes separated discrete objects in numerical and experimental tests, it is naturally used in continuous objects (extended target) such as the human body, where our proposed method can provide the range and Doppler-velocity profiles of the scattering centers on each human body part. The above characteristic has been partially demonstrated by the experimental test, assuming a real human walking scenario in Section VI-C. In this article, 24 and 76 GHz band radars are assumed in the simulation or experiment, because many radar equipment with these bands have been released in Japan, while 60, 77, or 79 GHz band is exceedingly used worldwide. However, the results, in Section V, assuming 76 GHz band, could be extrapolated to some extent to the above frequency ranges because changing carrier frequency would not have a significant impact on the results in the incoherent based WKD scheme, while the resolutions of $k_x$, $k_z$, and $v_{\mathrm{d}}$ are slightly changed. Note that, while this study focuses on millimeter-wave radar, assuming automobile or short-range sensing radar, lower frequency and wider band (e.g., 1–3 GHz) radar assuming through-wall applications has been intensively studied. In assuming such lower frequency and wideband radar, we consider that the proposed decomposition scheme would be relatively ineffective, compared with that of the higher frequency model because the $k$-space and velocity resolutions become lower. However, in the lower frequency band, a wider frequency band is available, and it is not necessary to introduce the proposed technique, and the original WKD works well, if we obtain an accurate range-$\tau$ profile, even in such a lower band, as demonstrated in [28].

## REFERENCES


[1] S. Guo, Q. Zhao, G. Cui, S. Li, L. Kong, and X. Yang, "Behind corner targets location using small aperture millimeter wave radar in NLOS urban environment," *J. Sel. Topics Appl. Earth Observ. Remote Sens.*, vol. 13, pp. 460–470, 2020.

[2] S. Guo, G. Cui, L. Kong, Y. Song, and X. Yang, "Multipath analysis and exploitation for MIMO through-the-wall imaging radar," *J. Sel. Topics Appl. Earth Observ. Remote Sens.*, vol. 11, no. 10, pp. 3721–3731, Oct. 2018.

[3] G. Gennarelli, R. Solimene, F. Soldovieri, and M. G. Amin, "Three-dimensional through-wall sensing of moving targets using passive multistatic radars," *J. Sel. Topics Appl. Earth Observ. Remote Sens.*, vol. 9, no. 1, pp. 141–148, Jan. 2016.

[4] Y. Song, J. Hu, T. Jin, Z. Li, N. Chu, and Z. Zhou, "Estimation and mitigation of time-variant RFI based on iterative dual sparse recovery in ultra-wide band through-wall radar," *J. Sel. Topics Appl. Earth Observ. Remote Sens.*, vol. 12, no. 9, pp. 3398–3411, Sep. 2019.

[5] H. Li, G. Cui, L. Kong, G. Chen, M. Wang, and S. Guo, "Robust human targets tracking for MIMO through-wall radar via multi-algorithm fusion," *J. Sel. Topics Appl. Earth Observ. Remote Sens.*, vol. 12, no. 4, pp. 1154–1164, Apr. 2019, doi: 10.1109/JSTARS.2019.2901262.

[6] X. Bai, Y. Hui, L. Wang, and F. Zhou, "Radar-based human gait recognition using dual-channel deep convolutional neural network," *IEEE Trans. Geosci. Remote Sens.*, vol. 57, no. 12, pp. 9767–9778, Dec. 2019.

[7] Y. Kim, S. Ha, and J. Kwon, "Human detection using Doppler radar based on physical characteristics of targets," *IEEE Geosci. Remote Sens. Lett.*, vol. 12, no. 2, pp. 289–293, Feb. 2015.

[8] M. Vahidpour and K. Sarabandi, "Millimeter-wave Doppler spectrum and polarimetric response of walking bodies," *IEEE Trans. Geosci. Remote Sens.*, vol. 50, no. 7, pp. 2866–2881, Jul. 2012.

[9] J. A. Nanzer and R. L. Rogers, "Human presence detection using millimeter-wave radiometry," *IEEE Trans. Microw. Theory Techn.*, vol. 55, no. 12, pp. 2727–2734, Dec. 2007.

[10] G. Li and P. K. Varshney, "Micro-Doppler parameter estimation via parametric sparse representation and pruned orthogonal matching pursuit," *J. Sel. Topics Appl. Earth Observ. Remote Sens.*, vol. 7, no. 12, pp. 4937–4948, Dec. 2014.

[11] L. Du, B. Wang, P. Wang, Y. Ma, and H. Liu, "Noise reduction method based on principal component analysis with beta process for micro-Doppler radar signatures," *J. Sel. Topics Appl. Earth Observ. Remote Sens.*, vol. 8, no. 8, pp. 4028–4040, Aug. 2015.

[12] M. Gustafsson, A. Andersson, T. Johansson, S. Nilsson, A. Sume, and A. Örbom, "Extraction of human micro-Doppler signature in an urban environment using a 'sensing-behind-the-corner' radar," *IEEE Geosci. Remote Sens. Lett.*, vol. 13, no. 2, pp. 187–191, Feb. 2016.

[13] Y. Kim and H. Ling, "Human activity classification based on micro-Doppler signatures using a support vector machine," *IEEE Trans. Geosci. Remote Sens.*, vol. 47, pp. 1328–1337, May 2009.

[14] L. Du, L. Li, B. Wang, and J. Xiao, "Micro-Doppler feature extraction based on time-frequency spectrogram for ground moving targets classification with low-resolution radar," *IEEE Sensors J.*, vol. 16, no. 10, pp. 3756–3763, May 2016.

[15] X. Qiao, T. Shan, R. Tao, X. Bai, and J. Zhao, "Separation of human micro-Doppler signals based on short-time fractional Fourier transform," *IEEE Sensors J.*, vol. 19, no. 24, pp. 12205–12216, Dec. 2019.

[16] P. Suresh, T. Thayaparan, T. Obulesu, and K. Venkataramaniah, "Extracting micro-Doppler radar signatures from rotating targets using Fourier-Bessel transform and time-frequency analysis," *IEEE Trans. Geosci. Remote Sens.*, vol. 52, no. 6, pp. 3204–3210, Jun. 2013.

[17] B. Boashash and P. O. Shea, "Polynomial Wigner-Ville distributions and their relationship to time-varying higher order spectra," *IEEE Trans. Signal Process.*, vol. 42, no. 1, pp. 216–220, Jan. 1994.

[18] F. Hlawatsch and G. F. Boudreaux-Bartels, "Linear quadratic time-frequency signal representations," *IEEE Signal Process. Mag.*, vol. 9, no. 2, pp. 21–67, Apr. 1992.

[19] Z. Sun, X. Li, W. Yi, G. Cui, and L. Kong, "Range walk correction and velocity estimation for high-speed target detection," in *Proc. IEEE Radar Conf.*, 2017, pp. 1478–1482.

[20] J. Xu, J. Yu, Y.-N. Peng, and X.-G. Xia, "Long-time coherent integration for radar target detection base on radon-Fourier transform," *Proc. IEEE Radar Conf.*, 2010, pp. 519–432.

[21] B. D. Carlson, E. D. Evans, and S. L. Wilson, "Search radar detection and track with the Hough transform, Part I: System concept," *IEEE Trans. Aerosp. Electron. Syst.*, vol. 30, no. 1, pp. 102–108, Jan. 1994.

[22] B. D. Carlson, E. D. Evans, and S. L. Wilson, "Search radar detection and track with the Hough transform, Part II. Detection statistics," *IEEE Trans. Aerosp. Electron. Syst.*, vol. 30, no. 1, pp. 109–115, Jan. 1994.

[23] B. D. Carlson, E. D. Evans, and S. L. Wilson, "Search radar detection and track with the Hough transform, Part III. Detection performance with binary integration," *IEEE Trans. Aerosp. Electron. Syst.*, vol. 30, no. 1, pp. 116–125, Jan. 1994.

[24] P. H. Huang, G. S. Liao, Z. W. Yang, and X. G. Xia, "Long-time coherent integration for weak maneuvering target detection and high-order motion parameter estimation based on keystone transform," *IEEE Trans. Signal Process.*, vol. 64, no. 15, pp. 4013–4026, Aug. 2016.

[25] Z. Sun, X. L. Li, W. Yi, G. L. Cui, and L. J. Kong, "Detection of weak maneuvering target based on keystone transform and matched filtering process," *Signal Process.*, vol. 140, pp. 127–138, May 2017.

[26] T. Zeng, C. Mao, C. Hu, and W. Tian, "Ground-based SAR wide view angle full-field imaging algorithm based on keystone formatting," *J. Sel. Topics Appl. Earth Observ. Remote Sens.*, vol. 9, no. 6, pp. 2160–2170, Jun. 2016.

[27] C. Pang, S. Liu, and Y. Han, "Coherent detection algorithm for radar maneuvering targets based on discrete polynomial-phase transform," *J. Sel. Topics Appl. Earth Observ. Remote Sens.*, vol. 12, no. 9, pp. 3412–3422, Sep. 2019.

[28] M. Setsu, T. Hayashi, J. He, and S. Kidera, "Super-resolution doppler velocity estimation by kernel-based range- $\tau$ point conversions for UWB short-range radars," *IEEE Trans. Geosci. Remote Sens.*, vol. 58, no. 4, pp. 2430–2443, Apr. 2020.

[29] T. Hayashi and S. Kidera, T. Hayashi, and S. Kidera, "BI-directional processing algorithm with RPM and WKD based Doppler velocity estimator for 3-D Doppler-radar imaging," in *Proc. IEEE Int. Geosci. Remote Sens. Symp.*, 2020, pp. 2336–2339.

[30] T. Hayashi and S. Kidera, "Iterative data clustering algorithm of Doppler-associated RPM imaging for UWB human body imaging radar," in *Proc. Photon. Electromagn. Res. Symp.*, 2019, pp. 519–400.
[31] J. Capon, "High-resolution frequency-wavenumber spectrum analysis," *Proc. IEEE*, vol. 57, no. 8, pp. 1408–1418, Aug. 1969.
[32] Y. Akiyama, T. Ohmori, and S. Kidera, "k-Space decomposition-based 3-D imaging with range points migration for millimeter-wave radar," *IEEE Trans. Geosci. Remote Sens.*, vol. 59, no. 8, pp. 6637–6650, Aug. 2021.
[33] T. Ando and S. Kidera, "Super-resolution Doppler velocity and range estimator for short-range human recognition radar," in *Proc. IEEE Radar Conf.*, 2020, pp. 1–6.
[34] Y. Akiyama and S. Kidera, "Low complexity algorithm for range points migration based human body imaging for multi-static UWB radars," *IEEE Geosci. Remote Sens. Lett.*, vol. 16, no. 2, pp. 216–220, Feb. 2019.
[35] V. U. Zavorotny and A. G. Voronovich, "Comparison of geometric optics and diffraction effects in radar scattering from steep and breaking waves," in *Proc. IEEE Int. Geosci. Remote Sens. Symp.*, 2007, pp. 519–1350.
[36] H. J. Ng, R. Feger, and A. Stelzer, "A fully-integrated 77-GHz UWB pseudo-random noise radar transceiver with a programmable sequence generator in SiGe technology," *IEEE Trans. Circuits Syst. I*, vol. 61, no. 8, pp. 2444–2455, Aug. 2014.
[37] D. Pan *et al.*, "A 76-81-GHz four-channel digitally controlled CMOS receiver for automotive radars," *IEEE Trans. Circuits Syst. I*, vol. 68, no. 3, pp. 1091–1101, Mar. 2021.
[38] S. B. Yeap, X. Qing, and Z. N. Chen, "77-GHz dual-layer transmit-array for automotive radar applications," *IEEE Trans. Antennas Propag.*, vol. 63, no. 6, pp. 2833–2837, Jun. 2015.
[39] M. Chen, C. Chen, S. Y. Chien, and R. Sherony, "Artificial skin for 76-77 GHz radar mannequins," *IEEE Trans. Antennas Propag.*, vol. 62, no. 11, pp. 5671–5679, Nov. 2014.
[40] P. J. B. Morris and K. V. S. Hari, "Detection and localization of unmanned aircraft systems using millimeter-wave automotive radar sensors," *IEEE Sensors Lett.*, vol. 5, no. 6, pp. 1–4, Jun. 2021.
[41] J. Song, C. Cui, S. Kim, B. Kim, and S. Nam, "A low-phase-noise 77-GHz FMCW radar transmitter with a 12.8-GHz PLL and a frequency multiplier," *IEEE Microw. Wireless Compon. Lett.*, vol. 26, no. 7, pp. 540–542, Jul. 2016.
[42] B. Efron, T. Hastie, I. Johnstone, and R. Tibshirani, "Least angle regression," *Ann. Statist.*, vol. 32, no. 2, pp. 407–499, 2004.

**Takeru Ando** received the B.E. degree in communication engineering and informatics in 2020 from the University of Electro-Communications, Tokyo, Japan, where he is currently working toward the M.E. degree in communication engineering and informatics with the Graduate School of Informatics and Engineering.

His research interest includes signal processing and imaging for millimeter wave radar as well as its applications.

**Shouhei Kidera** (Senior Member, IEEE) received the B.E. degree in electrical and electronic engineering and the M.I. and Ph.D. degrees in informatics from Kyoto University, Kyoto, Japan, in 2003, 2005, and 2007, respectively.

Since 2009, he has been with the Graduate School of Informatics and Engineering, University of Electro-Communications, Tokyo, Japan, where is currently an Associate Professor. He was a Visiting Researcher with the Cross-Disciplinary Electromagnetics Laboratory, University of Wisconsin Madison, Madison, WI, USA, in 2016. He was a Principal Investigator of the PRESTO Program of Japan Science and Technology Agency (JST) from 2017 to 2021. His current research interest includes advanced radar signal processing or electromagnetic inverse scattering issue for ultrawideband (UWB) 3-D sensor or biomedical applications.

Dr. Kidera was the recipient of the 2012 Ando Incentive Prize for the Study of Electronics, 2013 Young Scientist's Prize by the Japanese Minister of Education, Culture, Sports, Science, and Technology (MEXT), and 2014 Funai Achievement Award. He is a Senior Member of the Institute of Electronics, Information, and Communication Engineers of Japan (IEICE), and a Member of the Institute of Electrical Engineering of Japan (IEEJ) and the Japan Society of Applied Physics (JSAP).